

Article

Combining Operando Techniques for an Accurate Depiction of the SEI Formation in Lithium-Ion Batteries

Michael Stich ^{1,*}, Jesus Eduardo Valdes Landa ¹, Isabel Pantenburg ², Falk Thorsten Krauss ², Christoph Baumer ¹, Bernhard Roling ² and Andreas Bund ¹

¹ Electrochemistry and Electroplating Group, Technische Universität Ilmenau, Gustav-Kirchhoff-Straße 6, 98693 Ilmenau, Germany

² Department of Chemistry, Philipps-Universität Marburg, Hans-Meerwein-Straße 4, 35032 Marburg, Germany

* Correspondence: michael.stich@tu-ilmenau.de

Abstract: Its crucial importance to the long-term operation of lithium-ion batteries has made the solid electrolyte interphase (SEI) the subject of intensive research efforts. These investigations are challenging, however, due to the very complex and fragile nature of this layer. With its typical thickness being in the range of some 10 nm and its chemical make-up being highly sensitive to even the smallest amounts of impurities, it becomes clear that artifacts are easily introduced in investigations of the SEI, especially if the measurements are performed *ex situ*. To help ameliorate these issues, we herein report a combination of non-destructive operando techniques that can be employed simultaneously in the same electrochemical cell to provide a plethora of physical, morphological, and electrochemical data on the macroscopic and microscopic scale. These techniques encompass atomic force microscopy (AFM), electrochemical quartz crystal microbalance with dissipation monitoring (EQCM-D), and impedance spectroscopy (EIS). This work focuses on how to combine these techniques in a single electrochemical cell, which is suitable to study SEI formation while avoiding noise, crosstalk, inhomogeneous SEI formation, and other pitfalls.

Keywords: SEI; operando; AFM; EQCM-D; EIS; battery characterization; lithium-ion battery



Academic Editor: Yong-Joon Park

Received: 21 February 2025

Revised: 14 March 2025

Accepted: 19 March 2025

Published: 21 March 2025

Citation: Stich, M.; Valdes Landa, J.E.; Pantenburg, I.; Krauss, F.T.; Baumer, C.; Roling, B.; Bund, A. Combining Operando Techniques for an Accurate Depiction of the SEI Formation in Lithium-Ion Batteries. *Batteries* **2025**, *11*, 117. <https://doi.org/10.3390/batteries11040117>

Copyright: © 2025 by the authors. Licensee MDPI, Basel, Switzerland. This article is an open access article distributed under the terms and conditions of the Creative Commons Attribution (CC BY) license (<https://creativecommons.org/licenses/by/4.0/>).

1. Introduction

When a lithium-ion battery is charged for the first time after assembly, its organic electrolyte decomposes at the anode surface due to it being operated outside its electrochemical stability window. The decomposition products form a layer on the anode surface, and this is termed the solid electrolyte interphase (SEI). A stable and highly passivating SEI is crucial to the battery's operation as it prevents further electrolyte decomposition while simultaneously maintaining sufficient lithium-ion conductivity for the intercalation and deintercalation of the underlying active materials. Since the development of the first model of the SEI by Peled in 1979 [1], a vast amount of scientific effort has been devoted to understanding its chemical composition, morphology, and physical properties and their interrelation with formation conditions, electrolyte compositions, substrate properties, etc., with the ultimate goal being the optimization of the SEI as it functions as one of the main linchpins in the development of longer lasting lithium-ion batteries. Despite its importance and the extensive investigations ongoing, several key questions about the SEI, like the growth and charge transport mechanisms, have not satisfactorily been answered to date. Obtaining a clear understanding of the SEI, however, is a challenging scientific endeavor. Firstly, the SEI is thin, only ranging from several nanometers to several tens of

nanometers [2–4] and, during its initial formation steps, it is not always clearly demarcated from the surrounding electrolyte. Additionally, the SEI is not made of a single component but is composed of various organic and inorganic phases [1], which, in turn, continue to react as the state-of-charge (SOC) changes [3] and the battery ages [2,5]. Small variations in the formation parameters [5] and the addition of small amounts of additives [6] or contaminants [7] to the electrolyte can have large effects on the SEI’s properties. Against this backdrop, it becomes evident that SEI investigations can easily be prone to measurement artifacts, especially those methods that are performed *ex situ* and require the rinsing or drying of the anode surface, which can lead to undesired alterations of the SEI. Also, exposure of the SEI to a vacuum, moisture, and/or the air, or the measurement techniques themselves, can change the SEI profoundly [8]. For example, Edström et al. [4] report that depth profiling by Ar⁺ sputtering can lead to the decomposition of Li₂CO₃ into Li₂O or the decomposition of LiPF₆ or LiBF₄ into LiF. Additionally, they report that air exposure of the SEI can lead to the increased presence of Li₂CO₃, while rinsing can wash away LiF crystals and trace amounts of HF can react with and, thus, reduce the amount of detected Li₂CO₃. HF, in turn, can be a product of the reaction of trace water amounts with LiPF₆ [9]. These results are consistent with findings by Schroder et al. [10], who reported more fluoride and oxygen containing species in the SEI of crystalline silicon electrodes after exposure to ambient air.

As several of these artifacts are difficult to avoid when using *ex situ* techniques, a good case can be made for using *in situ* techniques whenever possible. Next to the investigation methods taking place directly at the location of the SEI formation (*in situ*), it is, additionally, favorable to continuously obtain data during the formation experiment (*operando*). While *operando* investigations with various techniques, such as near-ambient pressure XPS [11], electrochemical AFM [12], acoustic techniques [13], time-slicing neutron reflectometry [14,15], and EQCM-D+EIS [16], have been reported, combinations of *operando* techniques that can provide electrochemical, physical, and morphological information on the SEI simultaneously in one cell are exceedingly rare. To further clarify open research questions on the SEI formation, there is a research need for combined setups that can provide a more holistic view of the SEI and reduce the number of experiments needed and time invested, while also reducing the possibility of accidental deviations in experimental conditions between experiments. In this work, we show how to combine AFM, EQCM-D, and EIS, all working *operando*, in an electrochemical cell, while avoiding noise and crosstalk between them, highlight possibilities regarding where artifacts could occur and present strategies for combatting them. AFM reveals the morphological evolution in the nm to μm range of the SEI during its formation and can, additionally, supply nanomechanical data, like modulus, adhesion, deformation, etc. [12,17]. The EQCM-D data can quantify mass changes caused by the SEI layer growth and provide information on the viscoelasticity and roughness of this layer, and, in combination with EIS measurements, can, additionally, reveal electrochemical properties like ohmic resistances, charge transfer resistances, double layer capacitances, and diffusion data [16,18]. The combined data provided by these methods can, thus, help to gain a clearer understanding of the SEI formation while minimizing experimental artifacts.

2. Materials and Methods

2.1. The Electrochemical Cell

The electrochemical cell designed for the simultaneous use of AFM, EQCM-D, and EIS (Figure 1) is a three-electrode cell using a coated quartz crystal as working electrode (WE), which also serves as the sensor of the EQCM-D. The quartz crystal has two electrodes, a larger one in contact with the electrolyte on the front side and a smaller electrochemically

inactive one on the backside. Both electrodes are contacted via spring-loaded pins integrated into the PEEK cell body (see Supplementary Materials). The quartz crystal can be coated with a variety of materials (e.g., copper, carbon, silicon, or gold) by physical vapor deposition methods to produce conductive and functional layers. Chromium or titanium interlayers improve adhesion. The counter electrode (CE) is a ring made from lithium metal (99.9% purity, Sigma-Aldrich, Burlington, MA, USA) placed circularly around the working electrode. Regarding a homogenous current distribution, the optimal position for a CE would be directly above the working electrode. This space, however, is occupied during the experiment by the AFM scan head, which hovers on top of the working electrode. The effect of the CE placement is investigated in later chapters of this work. The lithium metal ring has a small opening, allowing the introduction of a reference electrode (RE), which consists of a thin insulated copper wire from a wiring pencil with a lithium tip. The wire, the lithium ring, and the coated quartz crystal are in contact with the battery electrolyte, which fills the volume inside the electrochemical cell (electrolyte reservoir of ~1.5 mL). The lithium tip of the RE is produced *in situ* directly before the measurement by plating Li from the CE on the copper wire's uninsulated tip. On top of the CE, a stainless-steel current collector is placed in contact with the lithium ring, serving as a current collector and containing a circular recess which can be filled with solvent.

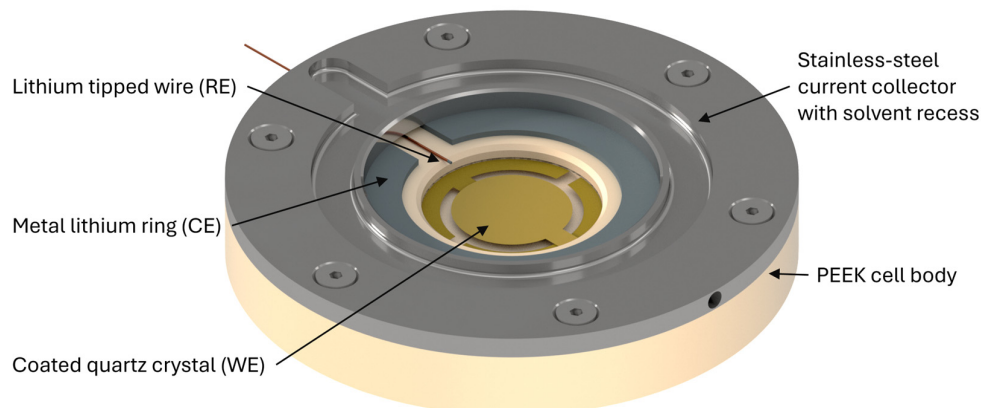


Figure 1. A CAD model of the electrochemical cell used for simultaneous AFM, EQCM-D, and EIS measurements. The inner compartment of the cell is filled with electrolyte during the experiment.

2.2. Electrolyte Evaporation Tests

The purpose of the solvent filled recess is to decrease the evaporation rate of the electrolyte. During an experiment, the AFM tip must scan freely over the sample, and so a small gap between the splash guard of the AFM scan head and the electrochemical cell is unavoidable in most systems (for details, see Supplementary Materials). The evaporation of solvent through this gap changes the electrolyte composition over time and, thus, limits the usable experiment duration significantly, limiting it to a few hours. Instead of refilling the evaporated solvent in the electrolyte reservoir directly, which would be difficult to do during uninterrupted AFM operation and cause undesired concentrations gradients in the cell, the recess is used. This recess, which is easily refillable without influencing the experiment and is not connected to the electrolyte reservoir of the electrochemical cell, is saturating the gas phase in the gap with solvent, which is supposed to decrease the evaporation rate of solvent from the electrolyte reservoir. To test the evaporation rates of the electrolyte reservoir, the mass loss of the electrochemical cell was determined. To measure the influence of the recess, the electrochemical cell was placed outside the glovebox in an ambient atmosphere, allowing for the use of a high-precision laboratory balance. Two cases were investigated. In the first experiment, only the electrolyte reservoir was filled

with 1.5 g of EC/DEC (1:1., *v/v*), while the solvent recess was left empty and the mass loss due to evaporation was measured over time. In the second experiment, additionally to the electrolyte reservoir, the solvent recess was also filled with DEC and the filling level marked and kept constant throughout the experiment so that all mass loss is assumed to originate from the electrolyte reservoir.

As the vapor pressure of EC is roughly 300 times lower than the vapor pressure of DEC (3.4 Pa [19] vs. 1065.8 Pa [20] at 20 °C), the evaporation is regarded as being dominated by DEC evaporation and the solvent recess should be filled with DEC during SEI experiments. Similar considerations can also be made for other lithium-ion battery electrolytes as the vapor pressures of linear carbonates (DEC, DMC, and EMC) is orders of magnitude higher than those of cyclic carbonates (EC, PC) [21]. Using a mixture of several linear carbonates in the battery electrolyte requires the recess to be filled with a mixture of those linear carbonates with their molar concentration being adjusted to their relative vapor pressures (Raoult's law).

2.3. The Setup Combining AFM with EIS and EQCM-D

The integration of the simultaneously operating operando techniques requires the elimination of noise and crosstalk between them. AFM is highly sensitive to mechanical vibration. The electrochemical cell is, therefore, placed on an active antivibration platform inside the glovebox. However, mechanical vibrations can still be introduced to the setup by using rigid, thick cables for the connection of the electrochemical cell. This can lead to strong image distortions during AFM operation, as displayed later. Thus, thin, non-shielded cables from a wiring pencil are utilized for the final ~10 cm of electrical connection to the electrochemical cell. The AFM images were taken in Bruker's Scan Asyst mode, a partially automated mode based on Peak Force Tapping, where on each pixel a very fast force curve is obtained. The used probe was based on a triangular silicon nitride cantilever with a tip of 20 nm nominal radius, which was termed Scan Asyst fluid. In addition to the mechanical vibrations, the electrical interference between the vector network analyzer (VNA), which analyses the impedance of the coated quartz crystal for the EQCM-D and the potentiostat, must be eliminated for a successful combined operation. As the signal generator of the VNA operates in the frequency range of the resonance frequency of the used quartz crystal (~5 MHz in this case), it can interfere with the feedback loop of the potentiostat, which is responsible for adjusting the current or voltage during the electrochemical experiment to the set value. The input impedance of the VNA can also affect EIS measurements (<1 MHz) if these devices are not effectively decoupled. To achieve this, a decoupler, based on a balun transformer (details in ref. [22]), splits the signals received from the front side of the coated quartz crystal (WE) into a high frequency branch connected to the VNA and a mid-to-low frequency branch connected to the potentiostat (Figure 2).

The effect of the electrical connections on the EIS data quality are investigated using an impedance test cell (Biologic) with known impedance characteristics, as displayed in Figure 3.

In the first setup, the impedance test cell was connected directly to the potentiostat with the manufacturer supplied cable, while in the second setup the test cell was connected in the glovebox, and in the third setup the VNA was included. In the fourth setup, the decoupler was added according to the schematic shown in Figure 4. The EIS measurements were carried out with a voltage amplitude of 10 mV in a frequency range from 200 kHz to 50 mHz with 10 measurement points per decade.

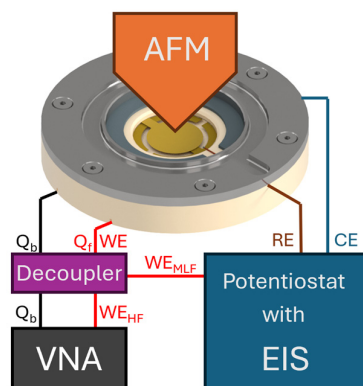


Figure 2. The combined setup showing the electrical connections of the potentiostat and the VNA and the position of the AFM scan head. (Q_f represents the front side of the coated quartz crystal, which also serves as WE, and Q_b its backside. The decoupler splits the WE signal into a high frequency signal WE_{HF} above ca. 1 MHz and a mid-to-low frequency WE_{MLF} signal below ca. 1 MHz.).

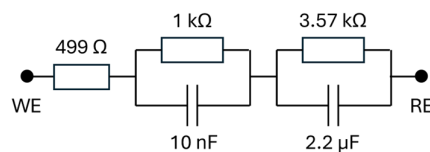


Figure 3. Equivalent circuit of the impedance test cell between WE and RE.

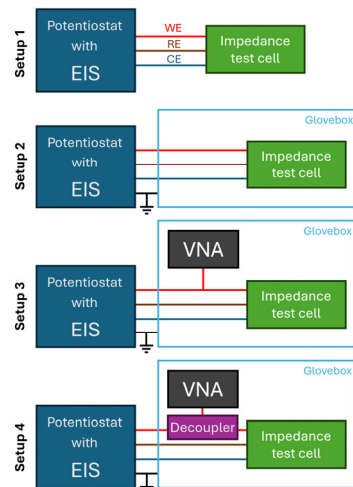


Figure 4. Schematics of the experimental setups to test the EIS signal quality.

Also, the quality of the EQCM-D data was investigated by checking for noise and distortion in the real and imaginary part of the admittance of the scattering parameter S11 in two setups, and in the stability and noise level of the frequency change over time. The resonance parameters can be extracted by fitting a phase shifted Lorentzian to these admittance curves [22]. Setup A consisted of a commercial quartz crystal holder, which is part of the setup of QCM200 System by Stanford Research Systems, connected to VNA and decoupler. This quartz crystal holder is not designed as a battery cell or for AFM operations. Setup B consisted of our electrochemical cell connected in the same way as Setup A. Both setups used the same gold-coated commercial quartz crystal with a nominal resonance frequency of 5 MHz.

The devices used were a Dimension Icon AFM (Bruker Co., Billerica, MA, USA) inside a MB 200B Glovebox (MBraun, Garching, Germany), a SP-240 potentiostat (Biologic, Seyssinet-Pariset, France), and a modified NanoVNA (originally designed by edy555. For

details on modification, see Supplementary Materials) as vectorial network analyzer for the EQCM-D analysis.

2.4. Current Distribution on the Working Electrode

The CE in this electrochemical cell is not placed directly above the WE (see above) because this space is occupied by the AFM scan head. Instead, the counter electrode is a lithium metal ring, which is placed in a slightly elevated position and surrounding the WE. This placement can lead to an inhomogeneous current distribution on the WE, which may result in significant differences in the SEI formation parameters, depending on the lateral position investigated. Simulations of the primary current density distribution, accounting for losses due to electrolyte resistance and secondary current density distribution and, additionally, considering the reaction kinetics, were carried out using the software COMSOL Multiphysics in version 6.2.0.415 to estimate the magnitude of current density variations and to find parameters minimizing this variation. Modeling the tertiary current distribution, which also takes mass transport into account, was not deemed to be necessary due to the very low current densities used in SEI formation and the high electrolyte concentration. For very fast SEI formation procedures, or for SEI formations in electrolytes of low concentration, this simplification would have to be re-evaluated. For the simulation, a simplified 3D model of the electrochemical cell was designed and converted to a triangle mesh with element sizes set as “extremely fine” (the model and its mesh quality is displayed in Supplementary Materials). Using the primary and secondary current distribution modules of COMSOL Multiphysics, the homogeneity of the current distribution on the cell was investigated. Additionally, the influence of an engaged AFM scan head was simulated and its effect on the homogeneity of the SEI deposition investigated. The kinetic parameters of the SEI reactions are not constant throughout the formation and depend on a variety of parameters, like the WE material and specific electrolyte composition. For this simulation, however, a rough estimate of the kinetic parameters is seen as sufficient for an estimation of the homogeneity of the SEI formation on the working electrode. The kinetic data for the SEI formation were taken from the detailed impedance analysis of graphite anodes in a 1 M LiPF₆ EC/DEC (3:7, v/v) electrolyte by Steinhauer et al. [23,24]. The charge transfer resistance (R_{ct}) of the SEI during the first formation cycle was calculated to be between ~172 and 861 Ωcm² (for details on R_{ct} calculation, see Supplementary Materials). The lower R_{ct} value, which is more unfavorable for homogeneous deposition, was used and converted to an exchange current density j_0 by applying Equation (1), which is valid for small overpotentials [25].

$$j_0 = \frac{RT}{FR_{ct}} \quad (1)$$

with R being the universal gas constant, T the temperature (293 K), and F the Faraday constant. The SEI formation current density was set to 50 μA/cm², according to values derived in preliminary experiments with this cell setup for formation times of ~10 h.

2.5. SEI Formation in the Combined Setup

To demonstrate the data that can be acquired simultaneously from the combined setup of AFM, EQCM-D, and EIS measurements, an initial SEI formation experiment is reported here. A quartz crystal coated with an amorphous carbon layer served as the working electrode in this experiment. The counter and reference electrode used were made of metallic lithium and an electrolyte 1 M LiPF₆ in EC/DEC (1:1, v/v) with 2 wt.% of vinylene carbonate (VC) was used. The SEI was formed on the working electrode according to the following procedure. After leaving the electrochemical cell at open circuit potential (OCP) for 20 min, the working electrode was cathodically polarized with a constant scan rate of 1 mV/s until it reached 2.0 V vs. Li/Li⁺, then the voltage was kept constant for another

20 min. This alternating pattern between cathodic polarization and a consecutive voltage plateau was maintained for the voltage steps 1.5 V, 1.25 V, 1.0 V, 0.8 V, 0.6 V, 0.4 V, and 0.2 V vs. Li/Li⁺. The dwell time of 20 min was chosen to allow for the comfortable capturing of two AFM images (2×512 lines/1 line/s = 17 min) at constant voltages during the voltage plateaus and for the EIS measurements to be performed at the end of the voltage plateaus, bringing those measurements closer to equilibrium conditions. In total, the experimental duration was ca. 4 h. Such a slow formation process was chosen as faster formation times lead to SEIs with undesired properties, such as poor transport characteristics [26]. AFM and EQCM-D data gathering remained active for the entire duration of the experiment, while EIS data gathering was only active at the end of the voltage plateaus. The AFM experiment was carried out with ScanAsyst fluid probes (Bruker Co., Billerica, MA, USA) made from silicon nitride with a denoted tip radius of 20 nm. The AFM data were obtained in the Peak Force Tapping mode. All displayed AFM images underwent a 1st order polynomial flattening procedure using the NanoScope Analysis software in version 1.50 (Bruker Co., Billerica, MA, USA), which only removes tilt from the image. The fast scan direction in all images is horizontal. An artificial shading filter was added to the AFM images to better visualize their three-dimensionality without changing the underlying data. The EIS experiment was carried out in a frequency range from 200 kHz to 50 mHz with an amplitude of 10 mV, recording 6 data points for each frequency decade. Each frequency sweep with the VNA encompassed 401 data points in a frequency span of 60 kHz. A few outliers (<20 of over 5000 measurement points) were removed from EQCM-D analysis. All devices used were the same as those mentioned in the above chapter.

3. Results and Discussion

3.1. Electrolyte Evaporation Tests

The results of the evaporation tests (Figure 5) show that the rate of EC/DEC (1:1, v/v) evaporation through the AFM gap is roughly 6.4% in two hours when no recess is used. Using the recess, the evaporation rate in an otherwise unaltered setup decreases to 1% per two hours, which is a decrease by a factor of ~6.6.

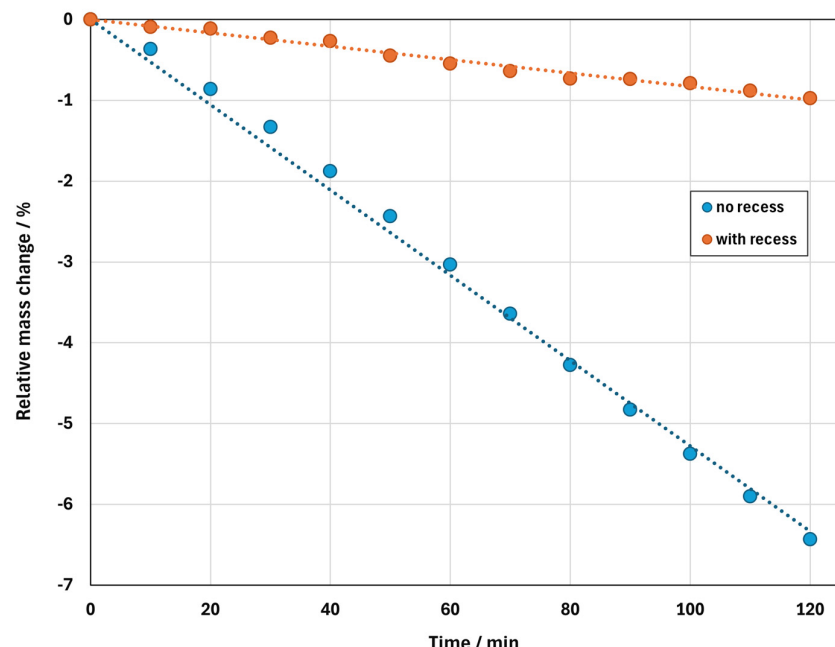


Figure 5. Mass loss due to evaporation in the electrochemical cell with and without the use of the solvent recess.

For the SEI formation experiments, the use of the solvent recess should significantly enhance the time of operation before the concentration in the electrolyte reservoir decisively changes. Therefore, in intervals (e.g., after an AFM image is captured), the reservoir should be replenished before it runs dry. This can be achieved without disturbing the experiment as a part of the solvent recess protrudes beyond the splash guard and is easily accessible.

3.2. The Setup Combining AFM with EIS and EQCM-D

3.2.1. Impedance

The impedance spectrum of the impedance test cell, consisting of a resistor and two RC elements in series, results in two right-shifted semicircles in the Nyquist plot, whose right-shift and diameters correspond to the resistance values of the resistors (Figure 3). Measuring a baseline impedance spectrum of this test cell directly at the potentiostat, using the manufacturer supplied cables (Figure 4—Setup 1), results in exactly these semicircles (Figure 6). When measuring the impedance test cell inside a glovebox, which requires adding a short distance of additional thin, non-shielded cables, the Nyquist spectra show only minimal deviation from the baseline spectra (Setup 2). It is advisable to connect the potentiostat's ground directly to the metal frame of the glovebox, otherwise the slightly different ground potentials of the potentiostat and the glovebox can lead to ground loops which may cause noise in the impedance data (see Supplementary Materials). Connecting the VNA to the working electrode cable of the impedance test cell, however, results in heavily distorted impedance data (Setup 3, full range, see Figure S3), which is dominated by the input impedance of the VNA instead of the impedance test cell. Without an effective separation of the EIS and EQCM-D signals, the combined simultaneous application of the two methods is, thus, not feasible. Adding the decoupler proves to be an effective method to separate those signals (Setup 4), with only minor deviations from the baseline.

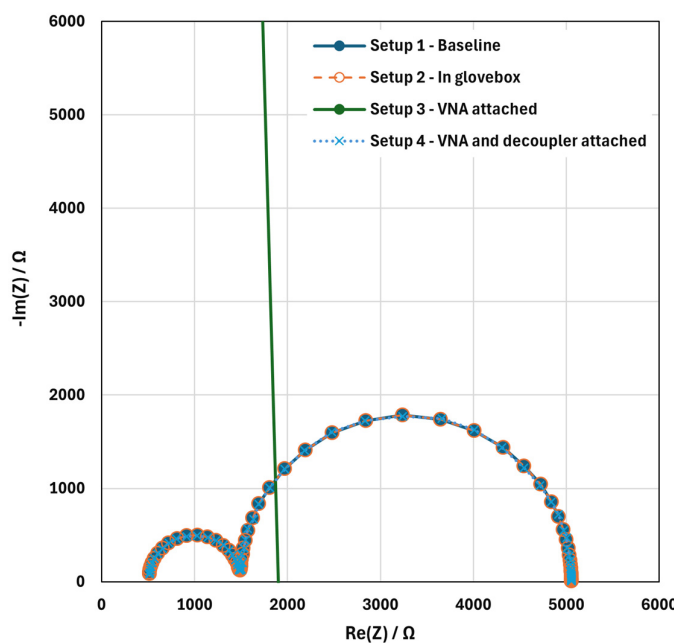


Figure 6. Nyquist plot of the impedance data for the tested setups (see Figure 3). Impedance data for Setup 3 lie outside the plot borders.

To quantify the deviation in the measured data from the ideal impedance spectrum based on the equivalent circuit, the measured data were fitted to the ideal impedance spectrum and the goodness of the fit was evaluated using a normalized Chi-squared test by calculating $\chi^2 / |Z|^2$. The results are provided in Table 1 and confirm the overall good

quality of the impedance data, with a minor decrease in Setup 4 with VNA and decoupler and non-meaningful results for the VNA connected without decoupler (Setup 3).

Table 1. Goodness of fit of the tested impedance setups displayed in Figure 6.

	$\chi^2 / Z ^2 / -$
Setup 1	3.55×10^{-4}
Setup 2	3.03×10^{-4}
Setup 3	N/A
Setup 4	1.52×10^{-3}

3.2.2. EQCM-D

The change in resonance frequency of the quartz crystal, Δf , over time in Figure 7c shows that very low drift values in the range of 1 Hz per hour are reached in both setups with a very low noise of <<1 Hz. A change of 1 Hz in resonance frequency corresponds to $\sim 18 \text{ ng/cm}^2$ of mass change according to the Sauerbrey equation, or a $\sim 0.2 \text{ nm}$ thickness change in a layer with a density of 1 g/cm^3 . Such a low drift and noise can be obtained in the dry atmosphere of a glovebox as moisture variations in the ambient atmosphere would usually result in more fluctuating adsorbed water layers on the quartz crystal leading to a less stable resonance frequency. Also, the damping of the quartz crystal, expressed here as the full bandwidth ($\omega = 2\Gamma$), shows a comparatively low drift and noise. The disturbance causing the sudden change in ω in Setup B by the small amount of ca. 0.7 Hz at around 26 min could not be observed during the experiment.

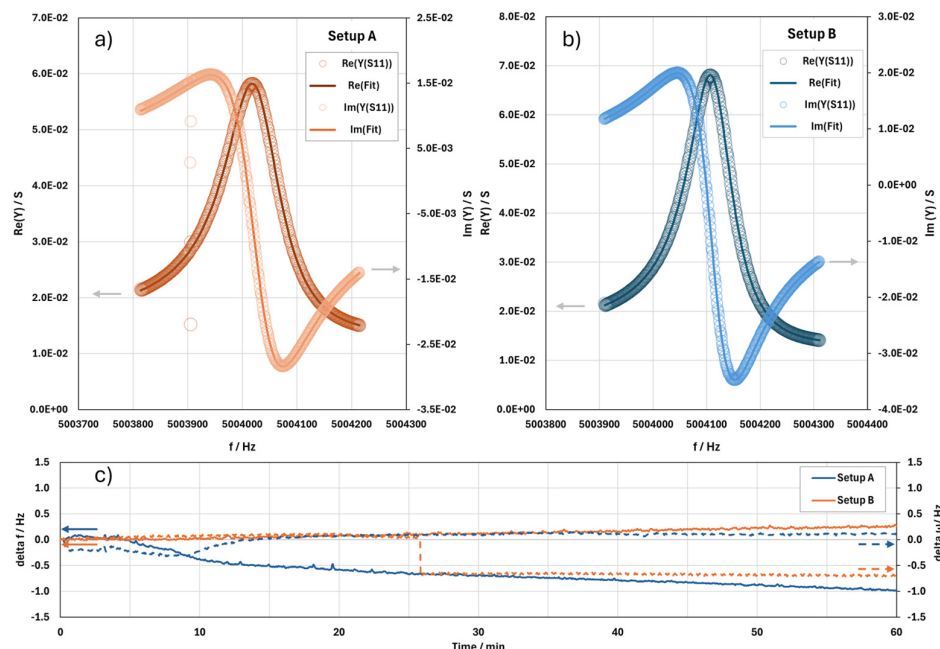


Figure 7. The real and imaginary part of the admittance Y of S11 and their fit with the phase shifted Lorentzian for the commercial quartz crystal holder (a) and our electrochemical cell (b) as well as the resonance frequency and damping change over time in both setups (c).

3.2.3. AFM

As the electronics of the AFM are insulated from the EQCM-D and EIS, the main point of concern here—next to the evaporation problem—is the mechanical introduction of noise, which can be effectively prevented using an active antivibration platform (Herzan, TS-140) and by designing cable connections to the cell with low mechanical stiffness so that the

vibrations of the glovebox and its components are not transmitted to the electrochemical cell. The effect of the used cables on this cell is shown in Figure 8 and highlights the importance of preventing mechanical noise transmission to the electrochemical cell.

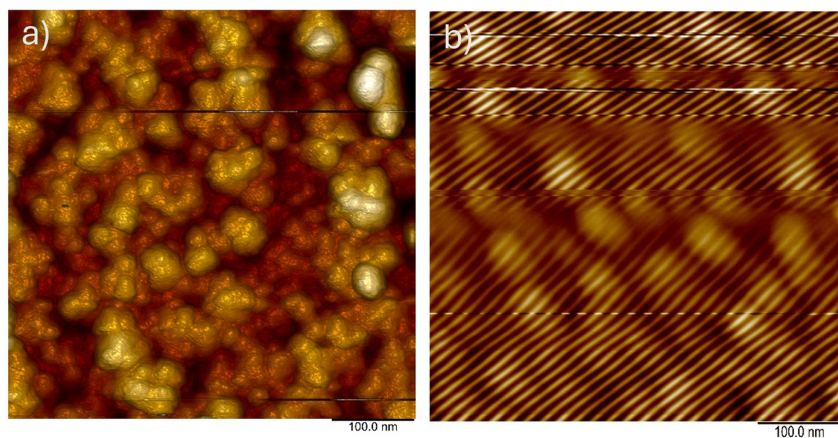


Figure 8. AFM images of a sample surface with the electrochemical cell electrically connected with (a) thin cables and (b) thick shielded cables. The mechanical noise introduced by the shielded cables causes significant artifacts in the AFM image.

3.2.4. Current Distribution on the Working Electrode

The simulation results show that the placement of the counter electrode around the working electrode indeed causes an inhomogeneous primary current density distribution due to the variable distance of the working electrode surface from the counter electrode (Figure 9a). The primary current density, only considering ohmic losses in the electrodes and the electrolyte, is, therefore, much higher at the edges of the working electrode than in its center. The moderate kinetics of the SEI formation, however, lead to a drastically different picture of the secondary current density distribution, with values between 45 and 59 $\mu\text{A}/\text{cm}^2$, which is much more homogeneous (Figure 9b). So, despite the non-ideal placement of the CE, a relatively homogeneous SEI formation, with a current density not more than 30% higher on the edges of the working electrode compared to its center, can be expected based on these simulation results.

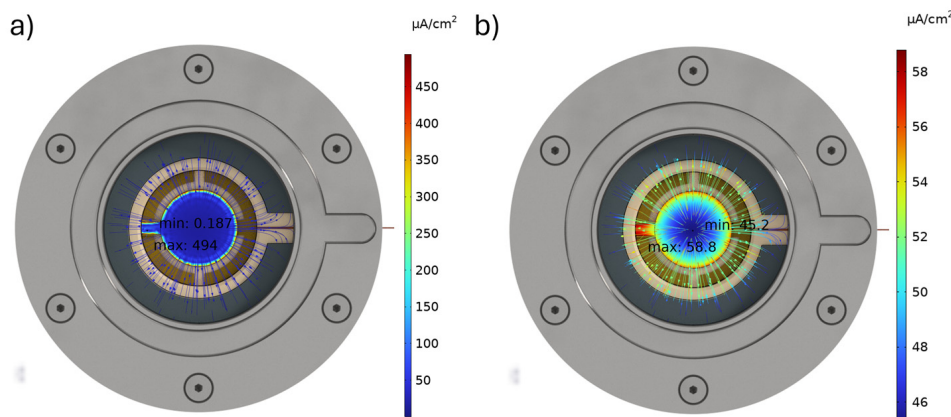


Figure 9. The simulated primary (a) and secondary (b) current density distribution on the working electrode.

Altering other factors in the simulation show, e.g., that a lower electrolyte filling level negatively influences the primary and secondary current density distribution (see Figure S6). Also, the introduction of the AFM scan head in the cell as an obstacle, as is the

case during AFM measurements, leads to a more inhomogeneous secondary current density distribution (see Figure S7). Here, the current density of the area directly underneath the scan head is only ca. half compared to the edge of the working electrode. If these deviations in current density are deemed too high for an accurate depiction of the SEI formation, it is recommended to only gather AFM data intermittently, e.g., during the latter parts of the constant voltage plateaus, where formation currents are lower and to keep the AFM scan head raised during the rest of the SEI formation.

3.2.5. SEI Formation in the Combined Setup

We hereafter present the first results of the SEI formation experiments. However, since the focus of this paper is primarily on the development and improvement of the combined methods, we will keep data discussion brief and will reserve the interpretation and comparison between different experimental conditions for a subsequent publication.

The EQCM-D data from this SEI formation experiment (Figure 10b) show that during the OCP period and the initial polarization steps until 2.0 V vs. Li/Li⁺, no apparent mass change occurs. The apparent mass change is calculated according to the Sauerbrey equation from the change in measured resonance frequencies (cf. Figure 7). Starting from below 2.0 V, however, the working electrode, first slowly and then more steadily, gains mass, which is mainly attributed to SEI formation and the build-up of a thick, viscous layer. With the increase in mass, the damping also increases, additionally indicating the growth of a highly viscous layer. Only in the later stages of the SEI formation below 0.4 V vs. Li/Li⁺ does the damping decrease again, which could indicate the formation of less viscous inorganic compounds. The impedance data for this three-electrode cell show semicircles in the Nyquist plot (Figure 10c), which continually decrease in diameter as the SEI formation procedure progresses. Similar behavior is known in the literature and is usually attributed to the decrease in interfacial resistance during the formation cycle [23]. The AFM images (Figure 10d) show a particle, possibly a LiF crystal, in their center. This prominent spot was used to continuously recenter the images throughout the measurement and, thus, observe the morphology evolution of the same surface location. While, until 1.0 V vs. Li/Li⁺, little morphological change in the surface occurs, subsequently, the surface changes more rapidly, gradually overgrowing the center particle. These surface morphology changes contrast with the mass and damping evolution monitored with EQCM-D, where a mass increase is already starting at higher potentials. We assume that this initial mass increase originates from the first decomposition reactions of the carbonate electrolyte. As those first reduction reactions may form soluble molecules like ethers, oligoethylene oxides, and fluorophosphates [2], the viscosity at the surface of the working electrode and electrolyte is assumed to increase, which adds to the oscillating mass of the quartz crystal and lowers its resonance frequency and increases its damping but does not lead to a changed surface morphology. At more reductive potentials (ca. <1 V), we then see the deposition and precipitation of the first solid components, which can also be picked up by the AFM measurement.

Overall, this combination of operando data provides a vast amount of reliable data, which is relevant for understanding the formation mechanisms of SEIs and their relation to experimental conditions better.

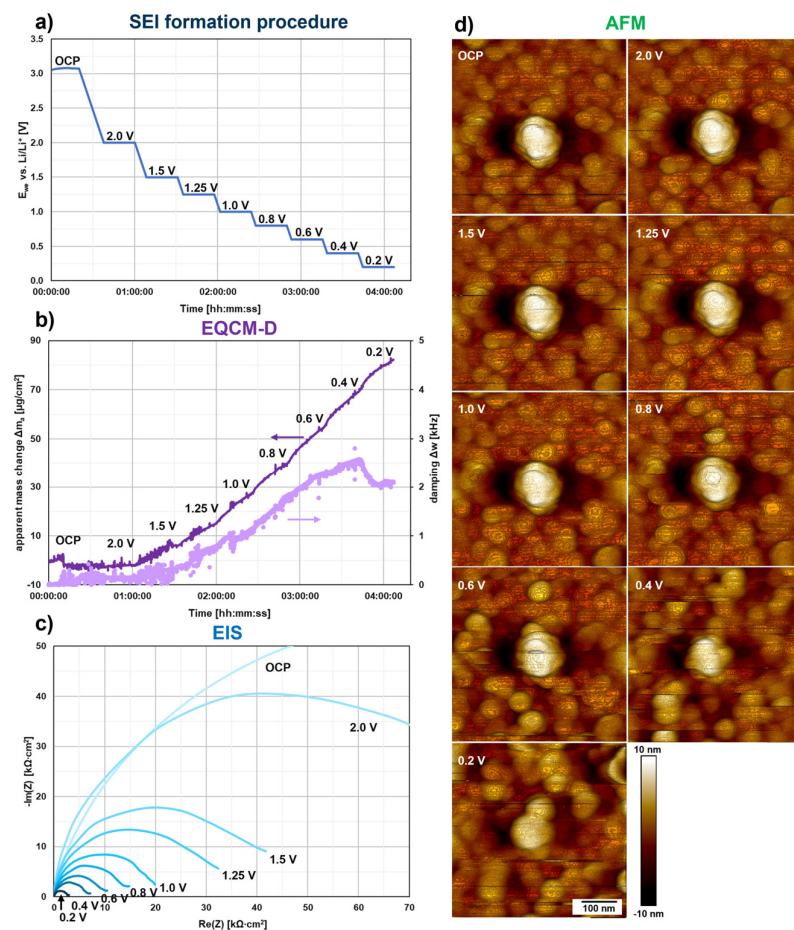


Figure 10. Resulting data on the SEI formation on an amorphous carbon coated quartz crystal in 1M LiPF₆ in EC/DEC (1:1, *v/v*) + 2 wt.% VC, showing the formation procedure (a), the apparent mass evolution and damping resulting from EQCM-D data (b), the electrical impedance data from the EIS measurements (c), and the morphological data from the AFM measurement (d). The scale bar and color bar displayed on the bottom AFM image are valid for all AFM images.

4. Conclusions

Combining several operando techniques in one electrochemical cell can help to avoid common measurement challenges and artifacts often encountered in ex situ techniques and allow for the generation of a multitude of relevant and accurate data, if performed correctly. Attention, however, should be paid to avoiding crosstalk between the different operando techniques and the introduction of noise. We have highlighted in this article various ways in which this can be achieved and have investigated the construction of an electrochemical cell suitable for investigating homogeneous SEI formation with an extended measurement duration. With the presented electrochemical cell, AFM, EIS, and EQCM-D data can be measured simultaneously and accurately. During the measurement with the AFM, electrolyte evaporation from the electrochemical cell occurs, which leads to undesired changes in the electrolyte concentration and, ultimately, to a limited measurement time. The measurement duration can be decisively extended with the integration of a solvent filled recess in the electrochemical cell, which saturates the gas phase in the gap and, thus, reduces the evaporation rate of the actual electrolyte reservoir. Tests with EC/DEC (1:1, *v/v*) have shown the evaporation rate to decrease by a factor of ~6.6. The recess is constructed to allow for easy solvent refill without causing concentration changes to the electrolyte reservoir.

Running EIS and EQCM-D simultaneously on the working electrode of the electrochemical cell is impractical unless the signals are split into a high frequency part, allowing for the transmission of data in the range of 5 MHz to the VNA of the EQCM-D, while allowing medium to low frequency data below 1 MHz to reach the potentiostat via a decoupler. It was shown that the use of the decoupler leads to nearly unaltered impedance data, EQCM-D data with low noise, and an excellent long-term stability of the resonance frequency. Adding AFM to EQCM-D and EIS requires the elimination of mechanical vibrations, most of which can already be avoided by using an active anti-vibration platform. But attention should be paid to stiff electrical connections to the cell, which can also transport mechanical vibration, causing considerable noise in AFM images.

As the AFM scan head needs to be placed directly above the WE, the CE must be integrated elsewhere. The presented electrochemical cell uses a ring-shaped Li-CE surrounding the WE. This suboptimal placement could possibly lead to a highly inhomogeneous SEI growth, which would render results from this cell challenging to interpret. To investigate this, simulations of the primary and secondary current density distribution were carried out and the results showed that the primary current density distribution is indeed very inhomogeneous. However, due to the moderate kinetics of the SEI formation, the secondary current density distribution is more homogeneous. Further simulation results also highlight that the secondary current density distribution becomes more inhomogeneous if the AFM scan head is introduced in the cell or the electrolyte filling level in the electrochemical cell is decreased.

With this paper, we show one way of integrating operando AFM, EQCM-D, and EIS in one single electrochemical cell and present the first results on a SEI formation, highlighting the potential insights that can be gained with such combined operando methods. We hope this work helps fellow researchers to avoid pitfalls when setting up similar combinations of operando techniques, be it for SEI investigations or in other fields.

Supplementary Materials: The following supporting information can be downloaded at: <https://www.mdpi.com/article/10.3390/batteries11040117/s1>.

Author Contributions: conceptualization, M.S., I.P., F.T.K., A.B. and B.R.; investigation, J.E.V.L. and M.S.; simulation, M.S. and C.B.; validation, C.B., I.P. and F.T.K.; writing—original draft preparation, M.S.; and writing—review and editing, all authors. All authors have read and agreed to the published version of the manuscript.

Funding: This research was funded by the Deutsche Forschungsgemeinschaft (DFG), grant numbers RO1213/18-1/BU1200/36-1. We acknowledge support for the publication costs from the Open Access Publication Fund of the Technische Universität Ilmenau.

Data Availability Statement: The original contributions presented in this study are included in the article and Supplementary Materials. Further inquiries can be directed to the corresponding author.

Acknowledgments: The authors would like to thank Diethelm Johannsmann and Christian Leppin for the valuable discussions on the EQCM-D setup and decoupler design and the mechanical workshop of the department of Electrical Engineering and Information Technology of TU Ilmenau for the manufacturing of the various iterations of the electrochemical cell.

Conflicts of Interest: The authors declare no conflicts of interest.

References

1. Peled, E. The Electrochemical Behavior of Alkali and Alkaline Earth Metals in Nonaqueous Battery Systems—The Solid Electrolyte Interphase Model. *J. Electrochem. Soc.* **1979**, *126*, 2047. [[CrossRef](#)]
2. Heiskanen, S.K.; Kim, J.; Lucht, B.L. Generation and Evolution of the Solid Electrolyte Interphase of Lithium-Ion Batteries. *Joule* **2019**, *3*, 2322–2333. [[CrossRef](#)]

3. Veith, G.M.; Doucet, M.; Baldwin, J.K.; Sacci, R.L.; Fears, T.M.; Wang, Y.; Browning, J.F. Direct Determination of Solid-Electrolyte Interphase Thickness and Composition as a Function of State of Charge on a Silicon Anode. *J. Phys. Chem. C* **2015**, *119*, 20339–20349. [[CrossRef](#)]
4. Edström, K.; Herstedt, M.; Abraham, D.P. A New Look at the Solid Electrolyte Interphase on Graphite Anodes in Li-Ion Batteries. *J. Power Sources* **2006**, *153*, 380–384. [[CrossRef](#)]
5. von Kolzenberg, L.; Stadler, J.; Fath, J.; Ecker, M.; Horstmann, B.; Latz, A. A Four Parameter Model for the Solid-Electrolyte Interphase to Predict Battery Aging during Operation. *J. Power Sources* **2022**, *539*, 231560. [[CrossRef](#)]
6. Michan, A.L.; Parimalam, B.S.; Leskes, M.; Kerber, R.N.; Yoon, T.; Grey, C.P.; Lucht, B.L. Fluoroethylene Carbonate and Vinylene Carbonate Reduction: Understanding Lithium-Ion Battery Electrolyte Additives and Solid Electrolyte Interphase Formation. *Chem. Mater.* **2016**, *28*, 8149–8159. [[CrossRef](#)]
7. Baakes, F.; Witt, D.; Krewer, U. Impact of Electrolyte Impurities and SEI Composition on Battery Safety. *Chem. Sci.* **2023**, *14*, 13783–13798. [[CrossRef](#)]
8. Malmgren, S.; Ciosek, K.; Lindblad, R.; Plogmaker, S.; Kühn, J.; Rensmo, H.; Edström, K.; Hahlin, M. Consequences of Air Exposure on the Lithiated Graphite SEI. *Electrochim. Acta* **2013**, *105*, 83–91. [[CrossRef](#)]
9. Stich, M.; Göttlinger, M.; Kurniawan, M.; Schmidt, U.; Bund, A. Hydrolysis of LiPF₆ in Carbonate-Based Electrolytes for Lithium-Ion Batteries and in Aqueous Media. *J. Phys. Chem. C* **2018**, *122*, 8836–8842. [[CrossRef](#)]
10. Schröder, K.W.; Celio, H.; Webb, L.J.; Stevenson, K.J. Examining Solid Electrolyte Interphase Formation on Crystalline Silicon Electrodes: Influence of Electrochemical Preparation and Ambient Exposure Conditions. *J. Phys. Chem. C* **2012**, *116*, 19737–19747. [[CrossRef](#)]
11. Capone, F.G.; Sottmann, J.; Meunier, V.; Ramírez, L.P.; Grimaud, A.; Iadecola, A.; Scardamaglia, M.; Rueff, J.-P.; Dedryvère, R. Operando Observation of the Dynamic SEI Formation on a Carbonaceous Electrode by Near-Ambient Pressure XPS. *Energy Environ. Sci.* **2024**, *17*, 1509–1519. [[CrossRef](#)]
12. Zhang, Z.; Smith, K.; Jervis, R.; Shearing, P.R.; Miller, T.S.; Brett, D.J.L. Operando Electrochemical Atomic Force Microscopy of Solid-Electrolyte Interphase Formation on Graphite Anodes: The Evolution of SEI Morphology and Mechanical Properties. *ACS Appl. Mater. Interfaces* **2020**, *12*, 35132–35141. [[CrossRef](#)] [[PubMed](#)]
13. Bommier, C.; Chang, W.; Li, J.; Biswas, S.; Davies, G.; Nanda, J.; Steingart, D. Operando Acoustic Monitoring of SEI Formation and Long-Term Cycling in NMC/SiGr Composite Pouch Cells. *J. Electrochem. Soc.* **2020**, *167*, 020517. [[CrossRef](#)]
14. Kawaura, H.; Harada, M.; Kondo, Y.; Kondo, H.; Suganuma, Y.; Takahashi, N.; Sugiyama, J.; Seno, Y.; Yamada, N.L. Operando Measurement of Solid Electrolyte Interphase Formation at Working Electrode of Li-Ion Battery by Time-Slicing Neutron Reflectometry. *ACS Appl. Mater. Interfaces* **2016**, *8*, 9540–9544. [[CrossRef](#)]
15. Steinhauer, M.; Stich, M.; Kurniawan, M.; Seidlhofer, B.-K.; Trapp, M.; Bund, A.; Wagner, N.; Friedrich, K.A. In Situ Studies of Solid Electrolyte Interphase (SEI) Formation on Crystalline Carbon Surfaces by Neutron Reflectometry and Atomic Force Microscopy. *ACS Appl. Mater. Interfaces* **2017**, *9*, 35794–35801. [[CrossRef](#)]
16. Kitz, P.G.; Lace, M.J.; Novák, P.; Berg, E.J. Operando EQCM-D with Simultaneous in Situ EIS: New Insights into Interphase Formation in Li Ion Batteries. *Anal. Chem.* **2019**, *91*, 2296–2303. [[CrossRef](#)]
17. Luchkin, S.Y.; Lipovskikh, S.A.; Katorova, N.S.; Savina, A.A.; Abakumov, A.M.; Stevenson, K.J. Solid-Electrolyte Interphase Nucleation and Growth on Carbonaceous Negative Electrodes for Li-Ion Batteries Visualized with in Situ Atomic Force Microscopy. *Sci. Rep.* **2020**, *10*, 8550. [[CrossRef](#)]
18. Kitz, P.G. A New Perspective on Interphase Formation in Li-Ion Batteries by Combined EIS & EQCM-D. Ph.D. Thesis, ETH Zurich, Zürich, Switzerland, 2019.
19. Pokorný, V.; Štejfa, V.; Fulem, M.; Červinka, C.; Růžička, K. Vapor Pressures and Thermophysical Properties of Ethylene Carbonate, Propylene Carbonate, γ -Valerolactone, and γ -Butyrolactone. *J. Chem. Eng. Data* **2017**, *62*, 4174–4186. [[CrossRef](#)]
20. Pokorný, V.; Štejfa, V.; Fulem, M.; Červinka, C.; Růžička, K. Vapor Pressures and Thermophysical Properties of Dimethyl Carbonate, Diethyl Carbonate, and Dipropyl Carbonate. *J. Chem. Eng. Data* **2017**, *62*, 3206–3215. [[CrossRef](#)]
21. Hess, S.; Wohlfahrt-Mehrens, M.; Wachtler, M. Flammability of Li-Ion Battery Electrolytes: Flash Point and Self-Extinguishing Time Measurements. *J. Electrochem. Soc.* **2015**, *162*, A3084. [[CrossRef](#)]
22. Johannsmann, D.; Langhoff, A.; Leppin, C. Studying Soft Interfaces with Shear Waves: Principles and Applications of the Quartz Crystal Microbalance (QCM). *Sensors* **2021**, *21*, 3490. [[CrossRef](#)] [[PubMed](#)]
23. Steinhauer, M.; Risse, S.; Wagner, N.; Friedrich, K.A. Investigation of the Solid Electrolyte Interphase Formation at Graphite Anodes in Lithium-Ion Batteries with Electrochemical Impedance Spectroscopy. *Electrochim. Acta* **2017**, *228*, 652–658. [[CrossRef](#)]
24. Placke, T.; Siozios, V.; Schmitz, R.; Lux, S.F.; Bieker, P.; Colle, C.; Meyer, H.-W.; Passerini, S.; Winter, M. Influence of Graphite Surface Modifications on the Ratio of Basal Plane to “Non-Basal Plane” Surface Area and on the Anode Performance in Lithium Ion Batteries. *J. Power Sources* **2012**, *200*, 83–91. [[CrossRef](#)]

25. Bard, A.J.; Faulkner, L.R.; White, H.S. *Electrochemical Methods: Fundamentals and Applications*, 3rd ed.; Wiley: Hoboken, NJ, USA, 2022.
26. Kranz, S.; Kranz, T.; Graubner, T.; Yusim, Y.; Hellweg, L.; Roling, B. Influence of the Formation Current Density on the Transport Properties of Galvanostatically Formed Model-Type Solid Electrolyte Interphases. *Batter. Supercaps* **2019**, *2*, 1026–1036. [CrossRef]

Disclaimer/Publisher’s Note: The statements, opinions and data contained in all publications are solely those of the individual author(s) and contributor(s) and not of MDPI and/or the editor(s). MDPI and/or the editor(s) disclaim responsibility for any injury to people or property resulting from any ideas, methods, instructions or products referred to in the content.